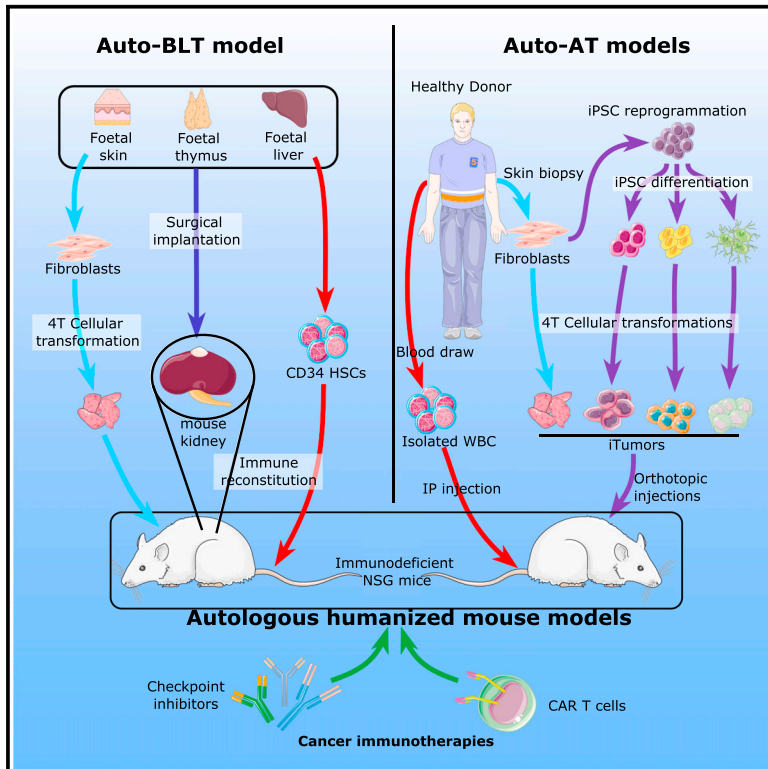


Autologous humanized mouse models of iPSC-derived tumors enable characterization and modulation of cancer-immune cell interactions

Graphical abstract



Authors

Gaël Moquin-Beaudry,
Basma Benabdallah,
Damien Maggiorani, ...,
Massimiliano Paganelli, Elie Haddad,
Christian Beausejour

Correspondence

c.beausejour@umontreal.ca

In brief

Inadequate mouse models limit the development and approval of anti-cancer drugs. Moquin-Beaudry et al. show that genetically defined tumors from primary and iPSC-derived cells recapitulate human immune cell activity when injected in autologous humanized mice, providing an approach to study cancer-immune cell interactions.

Highlights

- Many tumor types can be generated from iPSC-derived cells obtained from healthy donors
- These tumors are recognized by autologous immune cells in humanized mice
- Human immune cells become dysfunctional in the tumor microenvironment
- Blockade of PD-1 increases the tumor immune infiltration in humanized mice



Article

Autologous humanized mouse models of iPSC-derived tumors enable characterization and modulation of cancer-immune cell interactions

Gaël Moquin-Beaudry,^{1,2} Basma Benabdallah,¹ Damien Maggiorani,¹ Oanh Le,¹ Yuanyi Li,¹ Chloé Colas,^{1,3} Claudia Raggi,¹ Benjamin Ellezam,^{4,7} Marie-Agnès M'Callum,^{1,5} Dorothée Dal Soglio,^{6,7} Jean V. Guimond,⁸ Massimiliano Paganelli,^{1,5,9,10} Elie Haddad,^{1,3,10} and Christian Beausejour^{1,2,11,*}

¹Centre de Recherche du CHU Sainte-Justine, 3175 Côte Sainte-Catherine, Montréal, QC H3T 1C5, Canada

²Département de Pharmacologie et Physiologie, Montréal, QC, Canada

³Département de Microbiologie, Immunologie et Infectiologie, Montréal, QC, Canada

⁴Département de Neurosciences, Montréal, QC, Canada

⁵Département de Biologie Moléculaire, Montréal, QC, Canada

⁶Département de Pathologie et Biologie Moléculaire, Faculté de Médecine, Université de Montréal, Montréal, QC, Canada

⁷Département de Pathologie, CHU Sainte-Justine, Université de Montréal, Montréal, QC, Canada

⁸CIUSSS du Centre-Sud-de-l'Île-de-Montréal, Montréal, QC, Canada

⁹Division of Gastroenterology, Hepatology and Nutrition and Pediatric Liver Transplantation Program at CHU Sainte-Justine, Université de Montréal, Montréal, QC, Canada

¹⁰Département de Pédiatrie, CHU Sainte-Justine, Université de Montréal, Montréal, QC, Canada

¹¹Lead contact

*Correspondence: c.beausejour@umontreal.ca

<https://doi.org/10.1016/j.crmeth.2021.100153>

MOTIVATION Preclinical models capable of providing an environment where human tumors are confronted with autologous immune cells are not easily accessible. Even when possible, for example when using patient-derived xenografts, these tumors are not rejected following the injection of autologous human immune cells. This makes it impossible to study mechanisms that interfere with the tumor-immune response. As a solution, we generated genetically defined tumor cell lines from primary and iPSC-derived cells, which, when injected in autologous humanized mice, could be partially or totally rejected. Our models offer the advantage of generating several types of customizable autologous tumors from the same donor, providing a unique tool to study cancer-immune cell interactions.

SUMMARY

Modeling the tumor-immune cell interactions in humanized mice is complex and limits drug development. Here, we generated easily accessible tumor models by transforming either primary skin fibroblasts or induced pluripotent stem cell-derived cell lines injected in immune-deficient mice reconstituted with human autologous immune cells. Our results showed that fibroblastic, hepatic, or neural tumors were all efficiently infiltrated and partially or totally rejected by autologous immune cells in humanized mice. Characterization of tumor-immune infiltrates revealed high expression levels of the dysfunction markers Tim3 and PD-1 in T cells and an enrichment in regulatory T cells, suggesting rapid establishment of immunomodulatory phenotypes. Inhibition of PD-1 by Nivolumab in humanized mice resulted in increased immune cell infiltration and a slight decrease in tumor growth. We expect that these versatile and accessible cancer models will facilitate preclinical studies and the evaluation of autologous cancer immunotherapies across a range of different tumor cell types.

INTRODUCTION

Cancer drugs have the worst likelihood of approval compared with those of the rest of the industry (Hay et al., 2014). This situation underlines the need for better preclinical models to emulate

clinical conditions in a reliable manner (Johnson et al., 2001). This is particularly true in the era of immuno-oncology, where cancer is no longer viewed as a cell-autonomous disease. Instead, the whole tumor microenvironment, especially the host's immune system, is now considered an important



modulator of cancer development and elimination through cancer-immunoediting mechanisms (Dunn et al., 2004; Schreiber et al., 2011). Whereas classical cancer therapies have been shown to indirectly promote an anti-cancer immune response (Galluzzi et al., 2012, 2015), new immunotherapies such as checkpoint blockade inhibitors, vaccination, or chimeric antigen receptor (CAR) cell therapy aim at enhancing, potentializing, or inducing the host's anti-tumor immune response. However, very few preclinical models manage to provide a relevant immunological environment where human tumors are confronted with autologous immune cells.

Genetically engineered mouse models of cancer are valuable platforms, but their translational potential is limited by genetic and physiological differences between mice and humans (Mestas and Hughes, 2004; Balmain and Harris, 2000) and historically have demonstrated poor translational robustness (Hackam and Redelmeier, 2006). This has led to the development of various chimeric mouse models that use immunodeficient mice NOD/SCID/IL2R γ ^{null} (NSG) as vessels for human tumor growth. Patient-derived xenograft (PDX) models are powerful tools to study established tumors and were recently shown to be useful in predicting the response to PD-1 blockade (Voabil et al., 2021). Although PDX models are very potent tools to study established immune system-evading tumors, their use as preclinical platforms has some caveats such as maintenance, genetic drift, and, most importantly, their difficult combination with autologous immune cells. Some recent studies have tackled this issue by combining PDX with patient-derived hematopoietic stem cells (HSCs) or reinfusion of *in vitro*-expanded tumor-infiltrating lymphocytes (Fu et al., 2017; Jespersen et al., 2017; Voabil et al., 2021). However, the reliance on patient-derived immune cells limits the accessibility and scalability of such models. Similarly, although cancer cell lines are easy to use, they are debatably reproducible (Ben-David et al., 2018a, 2018b) and suffer the same complexities when it comes to studying the autologous tumor-immune system. To address this, human leukocyte antigen (HLA) matching has been successfully attempted but remains technically challenging (Wang et al., 2018).

Multiple approaches of mouse humanization are currently being used (Zitvogel et al., 2016). In humanized adoptive transfer (Hu-AT) models, mature and functional peripheral blood mononucleated cells (PBMCs) from donors are injected to immunodeficient mice for rapid and efficient reconstitution, albeit at the cost of a rapid graft versus host disease (GvHD) onset (King et al., 2008). Alternatively, humanization models using HSCs provide a long-term, robust human lymphocyte reconstitution (Mardon et al., 2009; Kooreman et al., 2017). However, effector T cells are trained on murine thymic tissue, undermining their ability to mount specific autologous T cell receptor (TCR) interactions. To address this, humanized bone marrow/liver/thymus models (Hu-BLT) employ fetal liver-derived HSCs with surgical implantation of autologous thymic tissue under the renal capsule for improved T cell education (Denton et al., 2010; Wahl and Victor Garcia, 2014).

Here, we propose an approach combining the flexibility of cancer cell lines obtained by transforming primary fibroblasts or induced pluripotent stem cell (iPSC)-derived cells with a set of defined oncogenes with the easy access to autologous im-

mune cells from healthy donors. Using either Hu-BLT or Hu-AT mice, we have developed versatile and accessible preclinical models that are uniquely positioned to study immune-naïve tumors in an autologous immune setting.

RESULTS

Engineered fibroblastic tumors are recognized by autologous immune cells in Hu-AT and Hu-BLT mice

In order to establish tumor models with easy access to autologous immune cells, we first elected to generate tumor cell lines from skin fibroblasts derived from healthy adult donors. Transformation of fibroblasts was achieved by successive lentiviral transductions of hTERT, SV40ER, and HRas^{v12} genes, which were shown to efficiently transform human cells (Hahn et al., 1999). These tumor cells were also tagged with the mPlum fluorescent marker for *in vivo* imaging and hereinafter designated the 4T cell line. The subcutaneous injection of tumor cells in the flank of NSG-SGM3 mice led to the formation of tumors in all mice within 3–4 weeks (Figure 1A). Previous work from our laboratory showed that adoptive transfer of PBMCs in NSG-SGM3 mice is highly effective at rejecting tumors and allogenic myoblasts (Benabdallah et al., 2020; Moquin-Beaudry et al., 2019). These naïve tumors were infiltrated by immune cells and partially or fully rejected following the adoptive transfer of 5×10^6 autologous human (Auto-AT) PBMCs and granulocytes (Figures 1A and 1B). We previously showed that injecting more PBMCs does not enhance tumor clearance (Moquin-Beaudry et al., 2019). Flow cytometry analysis of the immune infiltrate of residual tumors showed multiple immune cell populations, mostly restricted to T cells (Figures 1C and S1). Differential clustering analysis between human circulating and tumor-infiltrating immune cells (hTIIC) suggests that the tumor microenvironment can significantly alter the immune phenotype (Figure 1C, right). For example, tumors were enriched for CD14⁺ cells and immunosuppressive CD4⁺CD25⁺CD127⁻ Treg cells while depleted of effector CD56⁺ cells, CD8⁺ T cells, and CD45RO⁺ effector memory T cells (Figure 1D). However, no significant change in the proportion of dysfunctional T cells (defined as positive for the exhaustion markers T cell immunoglobulin and mucin domain-3 [Tim3] and programmed cell death protein 1 [PD-1]) was found, with all mice showing high levels of dysfunctional cells in both blood and the tumor environment (Figure 1E). Of note, high levels of exhaustion marker expression in circulating human immune cells were also observed in the absence of tumor growth, suggesting that it is an artifact of the AT model itself, possibly related to the progressive development of GvHD in these animals (data not shown). Still, we observed variations in the expression level (as detected by mean fluorescent intensity) of the exhaustion markers Tim3 and PD-1 between blood and tumor-infiltrating T cells (Figure 1F). These results suggest that while immune-naïve tumors are efficiently recognized by autologous immune cells, tumors are quickly able to induce an immunosuppressive microenvironment and avoid complete elimination in most cases.

We next wanted to measure the immunogenicity of fibroblastic tumors in Hu-BLT mice, which allow for a robust reconstitution of diverse functional immunological compartments. Using the

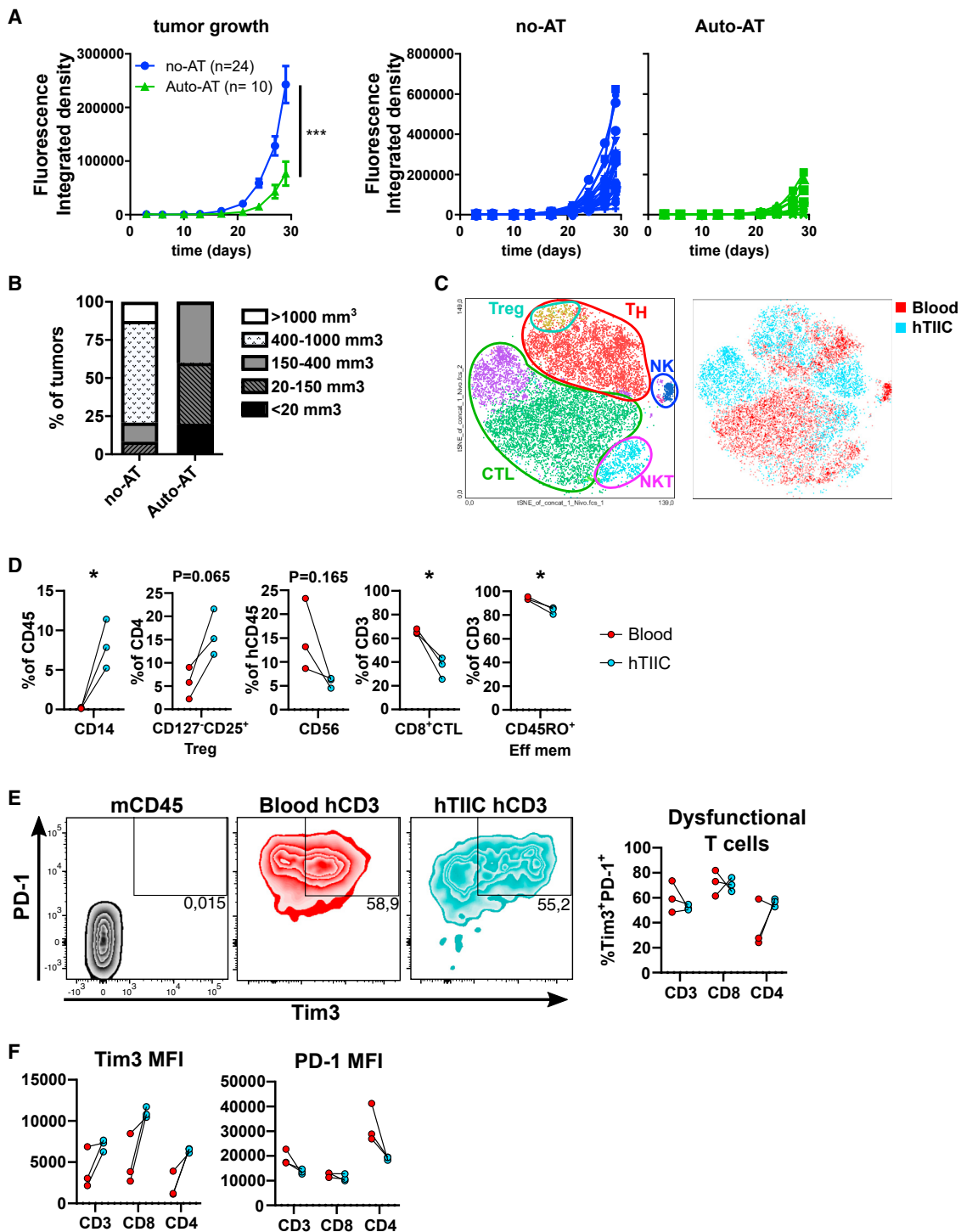


Figure 1. Engineered human skin fibroblast-derived tumors are recognized by autologous immune cells in Auto-AT mice

(A) Growth curves for 4T transformed adult dermal skin fibroblasts (left) and individual growth for all tumors without immune humanization (middle, no-AT, blue) and with autologous Hu-AT (right, Auto-AT, green) expressed in radiance integrated density. Shown is the mean \pm SEM.

(B) End point tumor volume assessment in no-AT (n = 24 tumors) and Auto-AT (n = 10 tumors) conditions.

(C) Characterization of the human immune infiltrate by flow cytometry. tSNE dimensional reduction visualization with unsupervised clustering using FlowSOM module for FlowJo and manual labeling of subtypes (left). Differential clustering between hTIIC and blood human CD45⁺ cells shows little overlap, signifying differential marker expression levels (right).

(D) Manual quantification of differentially represented human immune populations between blood and tumor samples.

(legend continued on next page)

same methodology used to generate 4T fibroblastic tumors derived from adult skin fibroblasts, we generated new 4T fibroblastic tumors derived from fetal skin. When injected into Hu-BLT mice, these tumors were partially or completely rejected in both allogeneic and autologous conditions (Figure 2A). As expected, the growth of allogeneic tumors was more efficiently inhibited than the growth of autologous tumors in Hu-BLT mice (Figures 2A and 2B). Flow cytometry analysis of the human immune compartment (Figures 2C, 2D, and S2) revealed no phenotypic variations in circulating human blood cells between mice harboring Auto- and Allo-tumors (Figures 2C, left, and 2E). hTIIC of non-eliminated tumors displayed similar population clustering with a slight but significant enrichment of CD8⁺ cells and a concomitant reduction in CD4⁺ cells in Auto-BLT tumors (Figures 2C, right, 2D, and 2E). As observed in Auto-AT mice, major phenotypic variations between circulating and tumor-infiltrating human immune cells were observed for both Auto- and Allo-BLT mice (Figures 2C–2E). However, whereas hTIIC displayed a marked increase in CD4⁺CD25⁺CD127⁻ Treg cells and in PD-1 and Tim3 expression, circulating T cells did not show any sign of exhaustion in opposition to what we observed in Auto-AT mice (Figures 2D and 2E). Yet, most tumors were eventually able to evade the immune response in Hu-BLT mice. Overall, these results demonstrate that it is possible to achieve partial or total immune rejection of engineered human fibroblastic tumor cells in humanized mice.

Tumors originating from transformed iPSC-derived hepatic cells are recognized by autologous immune cells in Hu-AT mice

To generate alternative tumor models that can be used in a humanized setting, we set out to transform iPSC-derived cells from healthy donors. First, iPSCs were differentiated into hepatocytes by using a previously described protocol (schematized in Figure 3A) (Raggi et al., 2020). We initiated the transformation process using SV40ER at different time points in the cell differentiation process, which led to the formation of growing colonies. These colonies were then transduced with HRas^{V12} and hTERT lentiviral particles after the differentiation protocol was completed and then finally modified to express the firefly luciferase marker (Figure 3A). We tried transforming cells at days 16, 22, and 30 of the differentiation protocol, which correspond to most of the cells being at the stage of progenitor, hepatoblast, and hepatocytes, respectively. We observed that the transformation potential was overall very limited, with progenitor cells forming few colonies (<10, transformation rate of approximately 0.01%), while only sporadic colonies emerged when cells had committed to the hepatoblast level. It was not possible to transform cells at day 30, when hepatocytes reach a quiescent state, suggesting that *in vitro* transformation using SV40ER is possible only in a subset of not yet fully differentiated cells and likely requires cells to maintain a proliferation potential.

Characterization by qPCR of untransformed hepatocyte-like cells (HLCs) showed that these cells express liver-specific markers (alpha fetoprotein [AFP], hepatocyte nuclear factor 4 alpha [HNF4A], albumin [Alb], and asialoglycoprotein receptor 1 [ASGR1]) at generally comparable levels compared with the control HepG2 hepatocellular carcinoma cell line (Figure S3). Upon transformation of HLCs (named HLC 4T), the expression of most markers was decreased (except for the bipotent hepatoblasts and cholangiocyte-associated cytokeratins 19 and 7), suggesting either that transformation induced dedifferentiation of the cells or that transformation occurred more efficiently in less differentiated progenitors. When injected intrahepatically (1 and 5 × 10⁵ cells for donor A and donor B, respectively), HLC 4T cells formed circumscribed tumors with entrapped liver parenchyma and mixed sarcomatoid components (Figure 3B, left). Tumor cells were highly mitotic, undifferentiated, pleomorphic, and occasionally hyperchromatic with some polynucleated cells and ill-defined cell borders (Figure 3B, right). AFP staining was weakly positive *in vitro* compared with the control HuH-6 hepatoblastoma cell line but negative *in vivo* (Figure S3, top), Alb expression was strongly positive *in vitro* and weakly positive *in vivo* (Figure S3, center), and HepPar1 staining was negative *in vitro* and *in vivo* (Figure S3, bottom). Pathological examination suggests that HLC 4T tumors resemble undifferentiated embryonic sarcoma of the liver (Putra and Ornvold, 2015). Interestingly, as observed with fibroblastic 4T cell lines, the intrahepatic injection of HLC 4T cells formed tumors in all animals with similar kinetics. The addition of 5 × 10⁶ autologous PBMCs and granulocytes was enough to partially or completely reject HLC 4T tumors in NSG-SGM3 mice in two independent donors (Figure 3C). These results suggest that it is possible to generate hepatic-like tumors and that these tumors are immunologically detected in Auto-AT mice.

iPSC-derived neural tumors recapitulate high-grade glioblastoma and are recognized by autologous immune cells in Hu-AT mice

To further explore the flexibility of our models, we initiated the transformation of iPSC-derived neural stem cells (iNSC) and astrocytes (iAstro). Cells were first differentiated using an established protocol (see Figure 4A and STAR Methods) and then characterized for their expression of key differentiation markers (Figure S4). The transformation of iNSC and iAstro (named iNSC 4T and iAstro 4T) was achieved using the same set of oncogenes described previously and initiated at a single time point immediately upon confirmation of the cells acquiring the nestin and glial fibrillary acidic protein (GFAP) markers, respectively. Transformed cells led to the generation of highly aggressive tumors when injected orthotopically in NSG-SGM3 mice (Figure 4B). As few as 1.5 × 10³ iAstro 4T cells were enough to consistently generate tumors within 3–4 weeks. iNSC 4T tumors also formed highly undifferentiated tumors in NSG-SGM3 mice

(E) Exhaustion/dysfunction gating strategy (left) and quantification (right) showing no significant change in total CD3, CD8⁺, and CD4⁺ T cell population dysfunction frequency between blood and tumor.

(F) Differential expression levels of dysfunction markers Tim3 and PD-1 on human T cell populations in blood vs. tumor samples shown by mean fluorescence intensity quantification. In (C, right), (D), (E), and (F), red indicates blood human immune cells, and light blue indicates hTIIC; n = number of tumors, two tumors per mouse.

(Figure 4B, top); however, the histopathology was inconclusive in characterizing them as classical glioblastomas multiform (GBM) (Figure S5). They were nonetheless highly proliferative tumors with prominent growth along Virchow-Robin spaces but with a limited diffuse infiltration and a distinctive accumulation near the dentate gyrus in all animals (Figure 4B, top). In contrast, iAstro 4T tumors were also highly proliferative but displayed a more conspicuous diffuse infiltration, parenchymal entrapment, and ventricular and leptomeningeal dissemination along with extensions in the Virchow-Robin space. Variable anaplastic features and a significant involvement of reactive astrocytes were also observed (Figure 4B, middle and bottom). Morphologically, iAstro 4T tumors were polymorphic and harbored multiple characteristic structures such as myxoid material, pre-necrotic cells, karyorrhexic nuclei, cellular monstrosities/giant cells, and some regions akin to giant cell and epithelioid GBM. Immunophenotypically, iAstro 4T tumors were strongly vimentin positive and moderately cytokeratin AE1/AE3 positive (Figure S5, left column) and lacked expression for MAP2 and S100 (Figure S6). Olig2, CD56, desmin, and cytokeratin 19 were also found to be negative in these tumors (data not shown). Consistent with a previous study using a similar transformation approach, *in vivo* tumors lacked GFAP expression despite *in vitro* expression (Rich et al., 2001) (Figure S5). As observed with our other tumor types, iAstro 4T tumors from two independent donors were partially or fully rejected by Auto-AT (Figure 4D). In Auto-AT mice, both iAstro 4T and iNSC 4T orthotopic tumors were highly infiltrated by hCD45 cells, mostly CD8 T cells (Figures 4D and S5B). Little to no infiltration was observed in surrounding mouse tissue, suggesting a specific T cell-mediated anti-tumor response. These results demonstrate that it is possible to transform iPSC-derived neural cell lines and that these cells are infiltrated by autologous immune cells upon orthotopic injection in the brain of Hu-AT mice.

Anti-PD-1 immunotherapy in Hu-AT mice leads to increased immune infiltration and clearance of autologous tumors

On the basis of the observation that our 4T tumors expressed high levels of PD-L1 and MHC-1 (Figure 5A), we next investigated if Hu-AT mice with autologous 4T tumors would represent a good model to evaluate the efficacy of anti-PD-1 immunotherapy. Our results showed that treatments of Hu-AT mice with the blocking antibody Nivolumab led to a slight, but not significant, reduction in the size of fibroblastic tumors (Figure 5B). Yet, flow cytometry analysis showed a significant increase in the relative abundance of human CD45⁺ cells infiltrating tumors in Nivolumab-treated animals (Figure S7), an observation we

also confirmed by immunofluorescent staining (Figure 5D). However, further analysis revealed that Nivolumab did not significantly affect immune-population profiles either in blood or within tumors, as shown by highly overlapping populations in t-distributed stochastic neighbor embedding (tSNE) dimensionality-reduction plots (Figure S6). Only CD3⁺CD56⁺ NK cells were slightly decreased in abundance in blood samples of Nivolumab-treated animals (Figure S6A), and nearly all human infiltrating immune cells were CD3⁺ T cells (Figure S6B). No specific population enrichment was observed within the hTIIC compartment in Nivolumab-treated animals. Phenotypically, infiltrating T cells were also largely similar between animal groups, with only PD-1 staining varying significantly, presumably as a staining artifact due to steric interference by residual circulating Nivolumab. Because fibroblastic tumors proved to be generally more difficult to reject compared with HLCs and iAstro tumors (compare Figure 1A with Figure 3C or 4D), we repeated the injection of Nivolumab in mice with HLC 4T tumors. In conditions where these tumors were not fully rejected in Auto-AT mice, treatment with Nivolumab was able to significantly improve tumor rejection (Figure 5C). Because HLC 4T tumors from Nivolumab-injected mice never reached a size that would have permitted their surgical retrieval, it was unfortunately not possible to analyze the tumor-immune infiltrate in this model. Overall, these results suggest that the injection of Nivolumab in mice harboring PD-L1⁺-engineered autologous tumors can increase the infiltration of T cells and delay the growth of certain tumor types.

DISCUSSION

In this study, we generated genetically defined tumor cell lines from primary and iPSC-derived cells that, when combined with immune humanization of mice, can be used for the evaluation of cancer-immune cell interactions in an autologous setting. A key feature of our model is that it offers the possibility to generate various tumor types from the same donor. This allows comparison between the cancer-immune and/or cancer-drug responses independently of genetic confounding effects when tumors of different origins are collected from various donors. Our models also offer the advantage of measuring the role of any given putative immune checkpoint or gene of interest by performing gain- and/or loss-of-function studies in a controlled genetic background. For example, the versatility of the model allowed us, as a proof of concept, to compare the efficacy of Nivolumab against different tumor cell types. Indeed, the strong expression of PD-L1 in our 4T tumors was not surprising, given that RAS signaling was shown to stabilize PD-L1 mRNA (Coelho et al., 2017). We also unexpectedly

(C) tSNE dimensional-reduction plots of human blood (left) or tumor-infiltrating immune cells (hTIIC, right) for Allo-BLT (top) and Auto-BLT (bottom) flow cytometry samples. All immune cells are from the same donor.

(D) Population annotation of human immune populations in BLT-humanized mice. Combined results and population annotation from (C) (top) and expression of exhaustion markers PD-1 and Tim3 (bottom left and middle) and Treg-associated marker CD25 (bottom right). All these markers are enriched in the hTIIC samples.

(E) quantification of effector populations (top row) in blood and hTIIC samples of Auto-BLT (gray bars, filled circles) and Allo-BLT (empty bars and circles) samples. Enrichment of CD8⁺ cells and concomitant decrease in hCD4⁺ T cells in Auto-BLT was observed. Quantification of immunosuppressive Treg (bottom far left) and dysfunctional T cells (bottom center-left), and expression levels of PD-1 (bottom center-right) and Tim3 (bottom far right). No significant variation between immunosuppressive and dysfunction markers between Auto- and Allo-BLT samples was observed.

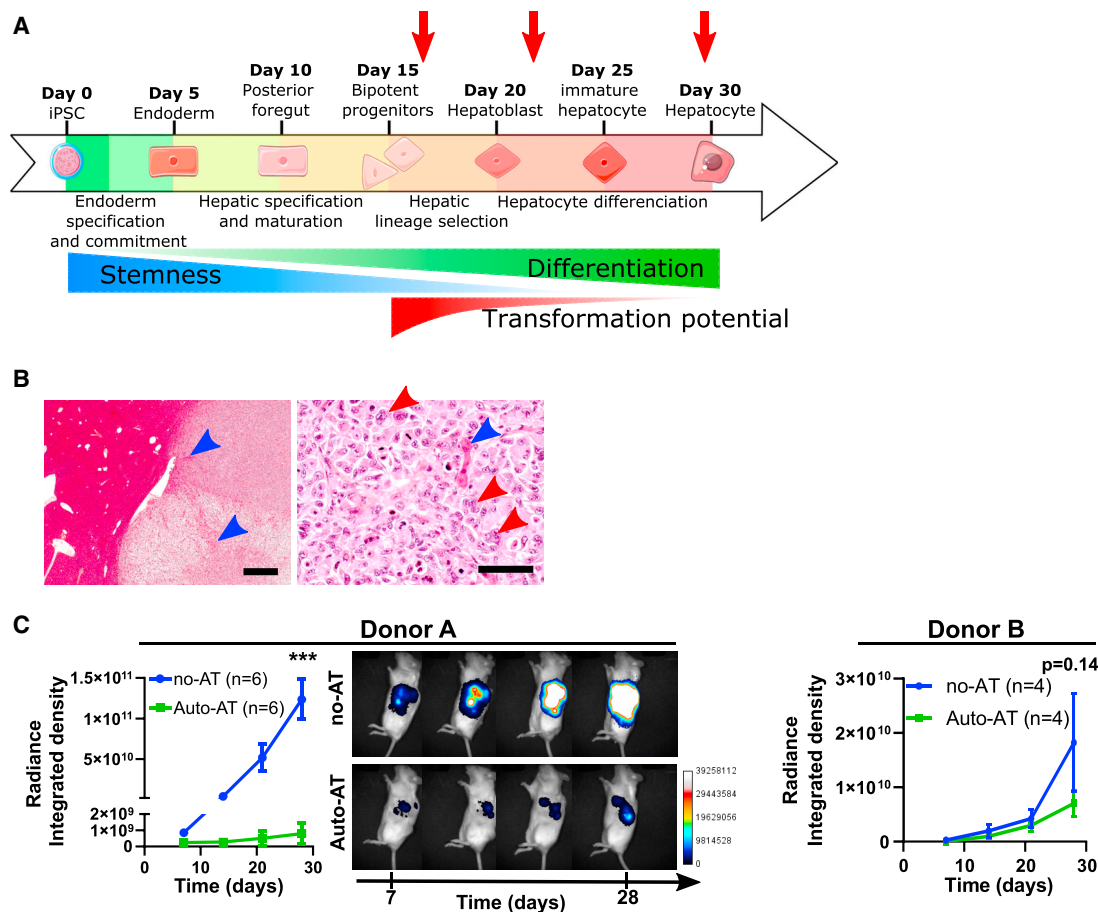


Figure 3. iPSC-derived hepatic tumors are recognized in Auto-AT mice

(A) Schematic of the iPSC differentiation protocol used to generate hepatocyte-like cells (HLC). Red arrows indicate time points for initiation of cellular transformation by SV40ER transduction.

(B) Histology of a HLC 4T tumor at low and high magnifications of hematoxylin-eosin-saffron (HES) staining. High magnification (left) shows border of well-circumscribed tumor with entrapped liver parenchyma (blue arrowheads) and varying tumor density. High magnification photomicrograph (right) again shows parenchymal entrapment (blue arrowheads), polynucleated cells (red arrowheads), numerous mitoses, hyperchromatic nuclei, and generally highly pleomorphic cells and nuclei.

(C) Mean \pm SEM of *in vivo* HCT 4T tumor elimination by Auto-AT. Integrated density of intrahepatic tumor-associated luciferase signal for two independent donors (left and right) and representative longitudinal *in vivo* bioluminescence from donor A. Scale bar in C: left, 1 mm; right, 100 μ m.

observed that iNSC and iNSC 4T tumors acquired the expression of the disialoganglioside GD2, a tumor-associated antigen (Figures S7A and S7B). This suggests that this tumor model could also be used for the testing of GD2-autologous chimeric antigen receptor T cells therapies. Others have shown that it is possible to identify markers predicting the response to PD-1 blockade using a PDX *in vitro* platform (Voabil et al., 2021). In comparison, our model is technically simpler, and human tissues are more accessible. Moreover, it can be customized to answer more fundamental questions. Indeed, since our iPSC-derived tumors have not been immune-edited and can be rejected following the AT of PBMC, our model could be used by anyone interested in performing a genetic screen for the identification of immune-resistance mechanisms or to evaluate the impact of specific modifica-

tions (for example, the accumulation of senescent cells in the tumor microenvironment).

Overall, we observed that fibroblastic tumors were less efficiently rejected compared with iPSC-derived hepatic and neuronal tumors. Besides the fact that these are intrinsically different tumors, other factors may explain this difference. We believe the subcutaneous injection of fibroblastic tumors, as opposed to intrahepatically or intracranially, likely limited the early access to immune cells, allowing the tumor to grow unchallenged, at least in the first few days/weeks. This hypothesis is supported by our observation that HLC-4T tumors were less efficiently rejected when injected subcutaneously compared with intrahepatically (data not shown). We therefore speculate that the inability of Nivolumab in enhancing the rejection of fibroblastic tumors is

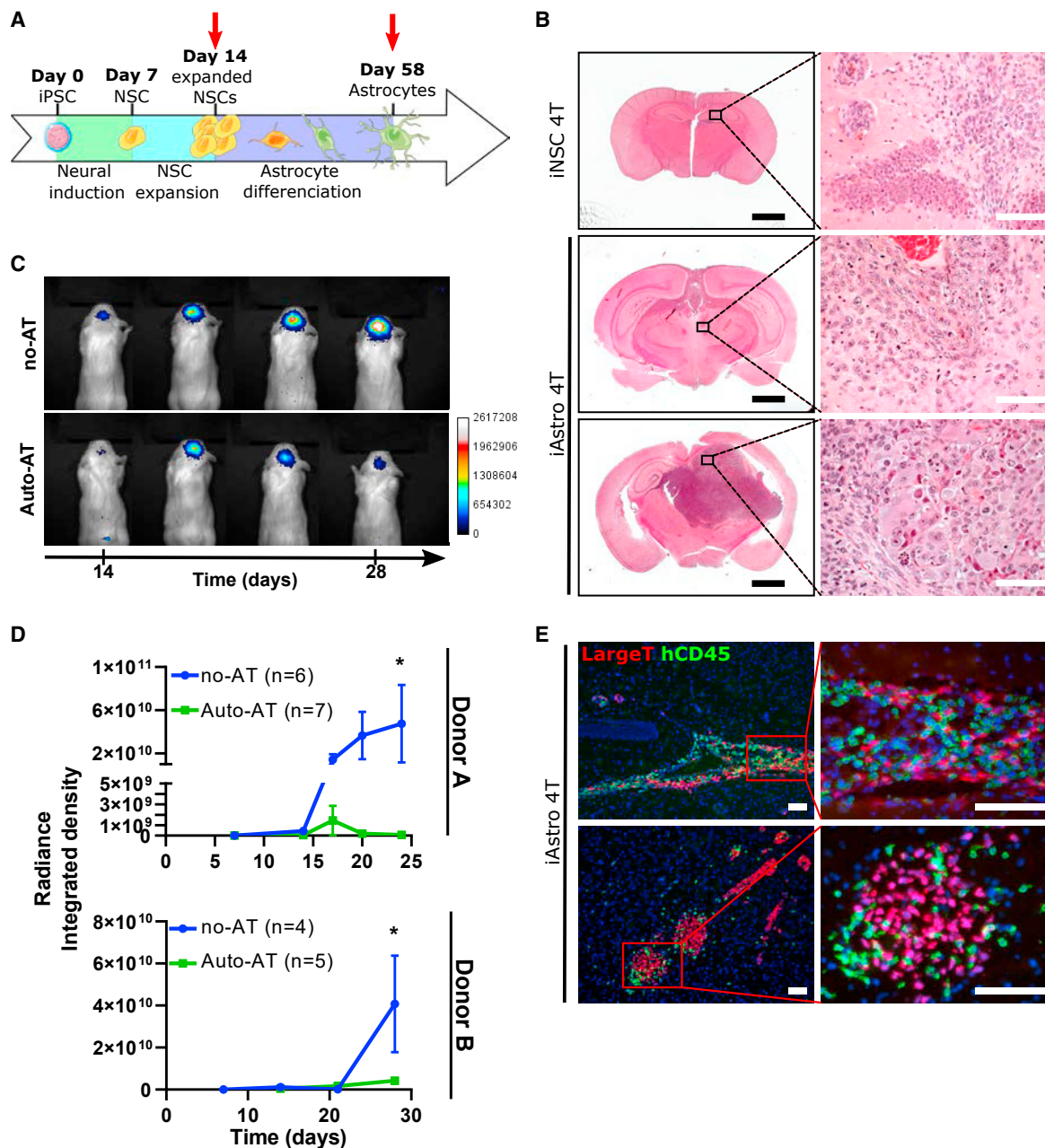


Figure 4. iPSC-derived neural tumors are rejected in Auto-AT mice

(A) Schematic of iPSC differentiation approach for the generation of neural stem cells (NSCs) and astrocytic cell populations. Red arrows indicate populations transformed using the 4T approach.

(B) Histology of one iNSC 4T tumor (top) and two representative iAstro-derived tumors (middle and bottom). High-magnification photomicrographs on right show poorly differentiated tumor cells with brisk mitotic activity with little (top) or more conspicuous (middle) diffuse infiltration or epithelioid/giant cell differentiation (bottom).

(C) Representative images of longitudinal *in vivo* luciferase imaging in no-AT (top) and Auto-AT (bottom) mice.

(D) Mean \pm SEM graph of *in vivo* luciferase signal quantification of iAstro 4T tumors with (Auto-AT) and without (no-AT) adoptive transfer in two different donors.

(E) Immunofluorescent staining images for human immune cells infiltrate detection within samples of iAstro 4T tumors at day 29 post-tumor-cell injection and Auto-AT showing human immune infiltrate specifically within tumors. Red, SV40 Large T; green, hCD45; blue, DAPI. Scale bar in B: left, 2 mm; all other scale bars, 100 μ m.

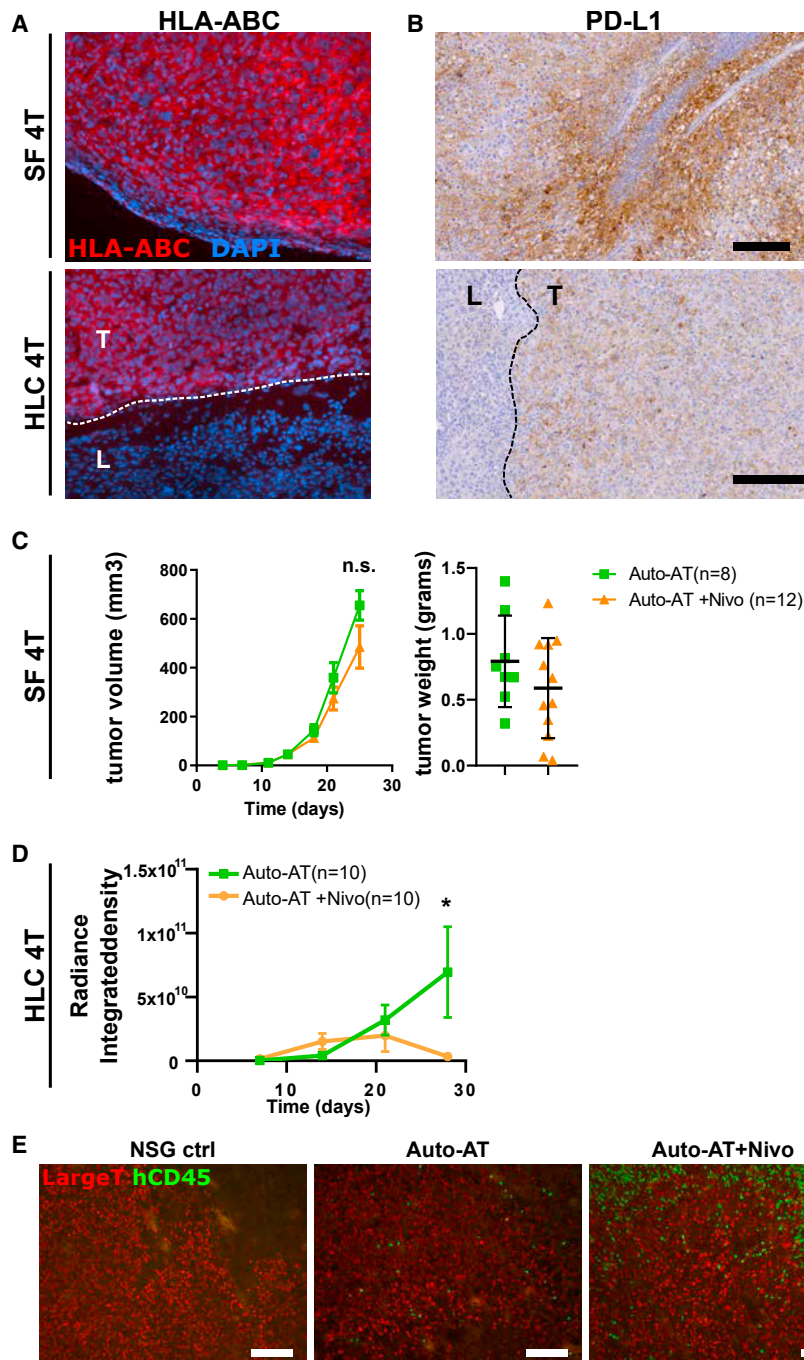


Figure 5. Injection of Nivolumab in Hu-AT mice leads to increased immune infiltration and clearance of autologous tumors

(A–B) Tumor microphotograph of HLA-ABC and PD-L1-stained fibroblastic (top) and HLC 4T (bottom) tumors. Fibroblastic tumors show strong PD-L1 staining, and HLC 4T tumors show tumor-specific (T) staining compared with surrounding mouse liver (L).

Effect of Nivolumab administration in Auto-AT fibroblastic (C) and HLC 4T (D) tumor-bearing mice.

(C) Shown are the results of two independent experiments showing tumor growth (left, mean \pm SEM) and tumor weight at sacrifice (right, mean \pm SD) for each experiment; n = number of tumors, two tumors per mouse.

(D) Tumor growth curve (mean \pm SEM) of HLC 4T tumors as measured by luciferase-associated radiance in Auto-AT (green), and Auto-AT treated with Nivolumab (orange); n = number of mice, one intrahepatic tumor injection per mouse.

(E) Representative images of human immune infiltrate within s.c. fibroblastic tumor samples for NSG-SGM3 control (left), Auto-AT alone (middle) and Auto-AT + Nivolumab (right). Red, large T; green human CD45. Scale bars, 200 μ m.

Yet, we noted the inability of this approach to transform quiescent cells *in vitro*, such as terminally differentiated HLC and GFAP-rich iAstro cells. Indeed, we observed that only experimental conditions containing residual proliferating cells were permissive to transformation by our oncogenes. This is in opposition to still-proliferating fibroblasts and NSC cultures, which were more uniformly transformed. Although this could be an artifact of non-physiologic cell culture conditions, this observation supports the hypothesis that most cancer cells originate from stem or progenitor cells rather than terminally differentiated quiescent cells (Visvader, 2011). In support of the cancer stem cell hypothesis, we noticed that transformed iAstro 4T cells expressed the glioblastoma cancer stem cell-associated marker CD133 *in vitro* (Singh et al., 2004) (Figure S7C). This is in contrast to what was previously observed using primary murine hepatic lineages where adult hepatocytes could be transformed using the HRas/SV40 oncogenes (Holczbauer et al., 2013). We speculate that a fraction of the murine adult hepatocytes may have been cycling when placed in culture in the presence of growth factors or simply that murine cells are more permissive than human cells to transformation.

likely the consequence of the tumor injection site rather than the choice of the tumor type or the humanized model used. How autologous immune-naïve tumors eventually resist immune clearance in both mouse models—whether because of immune exhaustion, modifications to the tumor microenvironment or any other possibilities—remains to be determined.

Here, we chose to work with an aggressive transformation approach (SV40ER/HRas^{V12}/hTERT), which systematically led to fast-growing, aggressive, and highly undifferentiated tumors.

The fact that all our cell lines generated with the 4T transduction approach were immunogenic to various degrees *in vivo* was intriguing. One explanation is that non-human proteins such as

the viral SV40 large and small T antigens or reporter proteins such as luciferase were immunogenic and elicited an immune response (Tatum et al., 2008; Day et al., 2014). However, it is also possible that such a broad transformation approach, which systematically led to poor differentiation phenotypes, as demonstrated with our HLC and iAstro 4T tumors, induced immunogenic tumor antigens, or that partially differentiated cells maintained the expression of embryonic antigens previously shown to be able to activate an immune response (Kooresman et al., 2018). If needed, it would be possible to generate autologous tumors free of any non-human antigens by transforming cells following prolonged exposure to carcinogens or by using only non-viral human genes (Kakunaga, 1978; Sasaki et al., 2009).

Both humanized mouse models used in this study (AT and BLT) were effective in mounting an autologous immune response mediated mostly by effector T cells. This is not surprising, given that other effector types are poorly reconstituted in most humanized models. NK cells, for instance, require exogenous (Huntington et al., 2009) or transgenic addition of IL-15 (Herndler-Brandstetter et al., 2017) or IL-2 (Katano et al., 2015) for their development and maturation in HSC-reconstituted mice. In this study, however, we suspect NK cells to be non-essential to tumor recognition and elimination for a few reasons. First, while CD3⁺CD56⁺ NK cells were identified in some Auto-AT animals, not surprisingly none were detected within tumors in the absence of cytokines supporting NK cell expansion. Also, the inability of BLT mice in the NSG background to reconstitute functional NK cells (Wege et al., 2008) did not prevent them from mounting an anti-tumor response similar to what we observed in AT mice. Finally, NK cells purified from peripheral blood failed to show a cytotoxic response against fibroblastic tumors *in vitro* (data not shown). Overall, given the complexity in generating BLT mice and despite the fact that T cells in our AT mice showed activation/exhaustion profiles, suggesting that the mice were at an early stage of GvHD, we believe researchers should use the Hu-AT model and especially that newly developed MHC knockout mouse strains should help circumvent GvHD in the future and allow for the long-term tracking of tumor growth (Ashizawa et al., 2017; Brehm et al., 2018).

Limitations of the study

Compared with patient-derived cancer cell lines or xenograft, our 4T tumors are more easily accessible, are genetically homogeneous, can be transformed using a customizable process, and have not undergone immunoediting events that can interfere with primary immune rejection. Although this represents a limitation for studying acquired immune resistance mechanisms, it can be advantageous for whoever is interested in screening for such mechanisms or validating new targets in a genetically defined environment.

Going forward, we propose that alternate tailoring of driver genetic alterations could improve different aspects of tumor phenotype and maintain tumor cells at a higher level of differentiation. For examples, driver mutations such as IDH1, ATRX, and EGFR in glioblastoma or CTNNB1, NFE2L2, APOB, and ALB in hepatocellular carcinomas could help steer these models toward the desired histopathology (Bailey et al., 2018). In this study, we limited the characterization of 4T tumors to key markers by using

histology and qPCR. It could be interesting to compare the whole gene expression signature of these tumors with the profile found in patient-derived cancers, keeping in mind that these profiles will be heterogeneous based on the donor itself, the differentiation state of the transformed cells, or the origin of the cancer. iPSC-derived tumors from many different donors and transformation protocols will need to be generated before we can adequately compare gene expression signatures. In the future, more adapted transformation protocols combined with the development of cancer organoid may be more representative of spontaneously emerging human tumors (Smith and Tabar, 2019). It remains to be determined whether iPSC-derived tumors generated using exclusively human genes or carcinogens would still be efficiently recognized by autologous immune cells. The robustness with which our tumors were recognized, despite the relatively limited T cell receptor repertoire injected in each mouse, suggests that at least a common major antigen, either tumor specific, embryonic, or of exogenous nature, is shared among these unedited tumors. However, the possibility of combining gene-editing tools to recapitulate precise somatic mutations with novel humanized mouse models resistant to GvHD should also allow for the development of more faithful iPSC-derived cancer models (Koga et al., 2020; Smith and Tabar, 2019; Brehm et al., 2018).

In conclusion, we generated highly accessible and flexible autologous models of tumor-immune cell interactions that should facilitate the evaluation and development of cancer immunotherapies. We foresee that ongoing development in our ability to adequately differentiate human iPSCs into a variety of cell types and organoid, including hematopoietic stem/progenitor cells for immune reconstitution in mice, will open many more possibilities in the near future.

STAR★METHODS

Detailed methods are provided in the online version of this paper and include the following:

- KEY RESOURCES TABLE
- RESOURCE AVAILABILITY
 - Lead contact
 - Materials availability
 - Data and code availability
- EXPERIMENTAL MODEL AND SUBJECT DETAILS
 - Animals and cell lines
- METHOD DETAILS
 - Hepatocyte differentiation
 - NSC and astrocyte differentiation
 - Lentivirus production
 - Cellular transformation
 - Orthotopic injections and monitoring
 - Histological analysis and staining
 - Immune infiltrate characterization
- QUANTIFICATION AND STATISTICAL ANALYSIS

SUPPLEMENTAL INFORMATION

Supplemental information can be found online at <https://doi.org/10.1016/j.crmeth.2021.100153>.

ACKNOWLEDGMENTS

We are grateful to the flow cytometry and animal facility for providing technical support and to Renée Dicaire for handling clinical samples.

This work was supported by a grant from la Fondation Charles Bruneau to C.B. and the Canadian Institutes of Health Research (MOP-102709). G.M.B. and D.M. were supported by a studentship from the Canadian Institutes of Health Research and a fellowship from le Fonds de recherche Santé Québec, respectively. The iPSC platform was supported by le réseau ThéCell du Fonds de la recherche Santé du Québec.

AUTHOR CONTRIBUTIONS

G.M.B., B.B., D.M., O.L., Y.L., M-A.M., and C.C. performed the experiments; C.R., M.P., and E.H. provided materials, reagents, and expertise; D.D.S. and B.E. provided expertise; J.V.G. provided materials; G.M.B. and C.B. designed the studies; G.M.B. and C.B. wrote the manuscript.

DECLARATION OF INTERESTS

The authors have no conflicts of interest to disclose. C.R. and M.P. are co-founders, shareholders, and officers of the regenerative medicine company Morphocell Technologies, Inc.

Received: June 8, 2021

Revised: November 3, 2021

Accepted: December 21, 2021

Published: January 14, 2022

REFERENCES

Ashizawa, T., Iizuka, A., Nonomura, C., Kondou, R., Maeda, C., Miyata, H., Sugino, T., Mitsuya, K., Hayashi, N., Nakasu, Y., et al. (2017). Antitumor effect of programmed death-1 (PD-1) blockade in humanized the NOG-MHC double knockout mouse. *Clin. Cancer Res.* **23**, 149–158.

Bailey, M.H., Tokheim, C., Porta-Pardo, E., and Cell, S.-S. (2018). Comprehensive characterization of cancer driver genes and mutations. *Cell* **173**, 371–385.e18.

Balmain, A., and Harris, C.C. (2000). Carcinogenesis in mouse and human cells: parallels and paradoxes. *Carcinogenesis* **21**, 371–377.

Beauséjour, C.M., Krtolica, A., Galimi, F., Narita, M., Lowe, S.W., Yaswen, P., and Campisi, J. (2003). Reversal of human cellular senescence: roles of the p53 and p16 pathways. *EMBO J.* **22**, 4212–4222.

Beier, K.T., Samson, M.E., Matsuda, T., and Cepko, C.L. (2011). Conditional expression of the TVA receptor allows clonal analysis of descendants from Cre-expressing progenitor cells. *Dev. Biol.* **353**, 309–320.

Ben-David, U., Beroukhim, R., and Golub, T.R. (2018a). Genomic evolution of cancer models: perils and opportunities. *Nat. Rev. Cancer* **19**, 97–109.

Ben-David, U., Siranosian, B., Ha, G., Tang, H., Oren, Y., Hinohara, K., Strathdee, C.A., Dempster, J., Lyons, N.J., Burns, R., et al. (2018b). Genetic and transcriptional evolution alters cancer cell line drug response. *Nature* **560**, 325–330.

Benabdallah, B., Désaulniers-Langevin, C., Colas, C., Li, Y., Rousseau, G., Guimond, J.V., Haddad, E., and Beauséjour, C. (2019). Natural killer cells prevent the formation of teratomas derived from human induced pluripotent stem cells. *Front. Immunol.* **10**, 2580.

Benabdallah, B., Desaulniers-Langevin, C., Goyer, M.L., Colas, C., Maltais, C., Li, Y., Guimond, J.V., Tremblay, J.P., Haddad, E., and Beauséjour, C. (2020). Myogenic progenitor cells derived from human induced pluripotent stem cell are immune-tolerated in humanized mice. *Stem Cells Transl. Med.* **10**, 267–277.

Brehm, M.A., Kenney, L.L., Wiles, M.V., Low, B.E., Tisch, R.M., Burzenski, L., Mueller, C., Greiner, D.L., and Shultz, L.D. (2018). Lack of acute xenogeneic graft-versus-host disease, but retention of T-cell function following engraft-

ment of human peripheral blood mononuclear cells in NSG mice deficient in MHC class I and II expression. *FASEB J.* **33**, 3137–3151.

Coelho, M.A., De Carne Trecesson, S., Rana, S., Zecchin, D., Moore, C., Molina-Arcas, M., East, P., Spencer-Dene, B., Nye, E., Barnouin, K., et al. (2017). Oncogenic RAS signaling promotes tumor immunoresistance by stabilizing PD-L1 mRNA. *Immunity* **47**, 1083–1099.e6.

Day, C.P., Carter, J., Weaver Ohler, Z., Bonomi, C., El Meskini, R., Martin, P., Graff-Cherry, C., Feigenbaum, L., Tuting, T., Van Dyke, T., et al. (2014). "Glowing head" mice: a genetic tool enabling reliable preclinical image-based evaluation of cancers in immunocompetent allografts. *PLoS One* **9**, e109956.

Denton, P.W., Krisko, J.F., Powell, D.A., Mathias, M., Kwak, Y.T., Martinez-Torres, F., Zou, W., Payne, D.A., Estes, J.D., and Garcia, J.V. (2010). Systemic administration of antiretrovirals prior to exposure prevents rectal and intravenous HIV-1 transmission in humanized BLT mice. *PLoS One* **5**, e8829.

Dunn, G.P., Old, L.J., and Schreiber, R.D. (2004). The three Es of cancer immunoeediting. *Annu. Rev. Immunol.* **22**, 329–360.

Fu, J., Sen, R., Masica, D.L., Karchin, R., Pardoll, D., Walter, V., Hayes, D.N., Chung, C.H., and Kim, Y.J. (2017). Autologous reconstitution of human cancer and immune system in vivo. *Oncotarget* **8**, 2053–2068.

Galluzzi, L., Buque, A., Kepp, O., Zitvogel, L., and Kroemer, G. (2015). Immunological effects of conventional chemotherapy and targeted anticancer agents. *Cancer Cell* **28**, 690–714.

Galluzzi, L., Senovilla, L., Zitvogel, L., and Kroemer, G. (2012). The secret ally: immunostimulation by anticancer drugs. *Nat. Rev. Drug Discov.* **11**, 215–233.

Gassen, S., Callebaut, B., Helden, M.J., Lambrecht, B.N., Demeester, P., Dhaene, T., and Saeys, Y. (2015). FlowSOM: using self-organizing maps for visualization and interpretation of cytometry data. *Cytometry A* **87**, 636–645.

Hackam, D.G., and Redelmeier, D.A. (2006). Translation of research evidence from animals to humans. *JAMA* **296**, 1731–1732.

Hahn, W.C., Counter, C.M., Lundberg, A.S., Beijersbergen, R.L., Brooks, M.W., and Weinberg, R.A. (1999). Creation of human tumour cells with defined genetic elements. *Nature* **400**, 464–468.

Hay, M., Thomas, D.W., Craighead, J.L., Economides, C., and Rosenthal, J. (2014). Clinical development success rates for investigational drugs. *Nat. Biotechnol.* **32**, 40–51.

Herndler-Brandstetter, D., Shan, L., Yao, Y., Stecher, C., Plajer, V., Lietzenmayer, M., Strowig, T., De Zoete, M.R., Palm, N.W., et al. (2017). Humanized mouse model supports development, function, and tissue residency of human natural killer cells. *Proc. Natl. Acad. Sci. U S A* **114**, E9626–E9634.

Holczbauer, A., Factor, V.M., Andersen, J.B., Marquardt, J.U., Kleiner, D.E., Raggi, C., Kitade, M., Seo, D., Akita, H., Durkin, M.E., and Thorgeirsson, S.S. (2013). Modeling pathogenesis of primary liver cancer in lineage-specific mouse cell types. *Gastroenterology* **145**, 221–231.

Huntington, N.D., Legrand, N., Alves, N.L., Jaron, B., Weijer, K., Plet, A., Corcuff, E., Mortier, E., Jacques, Y., Spits, H., et al. (2009). IL-15 trans-presentation promotes human NK cell development and differentiation in vivo. *J. Exp. Med.* **206**, 25–34.

Jespersen, H., Lindberg, M.F., Donia, M., Söderberg, E.M.V., Andersen, R., Keller, U., Ny, L., Svane, I.M., Nilsson, L.M., and Nilsson, J.A. (2017). Clinical responses to adoptive T-cell transfer can be modeled in an autologous immune-humanized mouse model. *Nat. Commun.* **8**, 707.

Johnson, J.I., Decker, S., Zaharevitz, D., Rubinstein, L.V., Venditti, J.M., Schempart, S., Kalyandrug, S., Christian, M., Arbuck, S., Hollingshead, M., and Sausville, E.A. (2001). Relationships between drug activity in NCI preclinical in vitro and in vivo models and early clinical trials. *Br. J. Cancer* **84**, 1424–1431.

Kakunaga, T. (1978). Neoplastic transformation of human diploid fibroblast cells by chemical carcinogens. *Proc. Natl. Acad. Sci. U S A* **75**, 1334–1338.

Katano, I., Takahashi, T., Ito, R., Kamisako, T., Mizusawa, T., Ka, Y., Ogura, T., Suemizu, H., Kawakami, Y., and Ito, M. (2015). Predominant development of mature and functional human NK cells in a novel human IL-2–producing transgenic NOG mouse. *J. Immunol.* **194**, 3513–3525.

King, M., Pearson, T., Shultz, L.D., Leif, J., Bottino, R., Trucco, M., Atkinson, M.A., Wasserfall, C., Herold, K.C., Woodland, R.T., et al. (2008). A new Hu-

- PBL model for the study of human islet alloreactivity based on NOD-scid mice bearing a targeted mutation in the IL-2 receptor gamma chain gene. *Clin. Immunol.* **126**, 303–314.
- Koga, T., Chaim, I.A., Benitez, J.A., Markmiller, S., Parisian, A.D., Hevner, R.F., Turner, K.M., Hessenauer, F.M., D'antonio, M., Nguyen, N.D., et al. (2020). Longitudinal assessment of tumor development using cancer avatars derived from genetically engineered pluripotent stem cells. *Nat. Commun.* **11**, 550.
- Kooreman, N.G., De Almeida, P.E., Stack, J.P., Nelakanti, R.V., Diecke, S., Shao, N.-Y., Swijnenburg, R.-J., Sanchez-Freire, V., Matsa, E., et al. (2017). Alloimmune responses of humanized mice to human pluripotent stem cell therapeutics. *Cell Rep.* **20**, 1978–1990.
- Kooreman, N.G., Kim, Y., De Almeida, P.E., Termglinchan, V., Diecke, S., Shao, N.Y., Wei, T.T., Yi, H., Dey, D., et al. (2018). Autologous iPSC-based vaccines elicit anti-tumor responses in vivo. *Cell Stem Cell* **22**, 501–513.e7.
- Marodon, G., Desjardins, D., Mercey, L., Baillou, C., Parent, P., Manuel, M., Caux, C., Bellier, B., Pasqual, N., and Klatzmann, D. (2009). High diversity of the immune repertoire in humanized NOD.SCID.gamma c-/- mice. *Eur. J. Immunol.* **39**, 2136–2145.
- Mestas, J., and Hughes, C.C. (2004). Of mice and not men: differences between mouse and human immunology. *J. Immunol.* **172**, 2731–2738.
- Moquin-Beaudry, G., Colas, C., Li, Y., Bazin, R., Guimond, J.V., Haddad, E., and Beausejour, C. (2019). The tumor-immune response is not compromised by mesenchymal stromal cells in humanized mice. *J. Immunol.* **203**, 2735–2745.
- Putra, J., and Ornvold, K. (2015). Undifferentiated embryonal sarcoma of the liver: a concise review. *Arch. Pathol. Lab.* **139**, 269–273.
- Raggi, C., M'callum, M.-A., Pham, Q.T., Gaub, P., Selleri, S., Baratang, N., Mangahas, C.L., Cagnone, G., Reversade, B., Joyal, J.-S., and Paganelli, M. (2020). Leveraging complex interactions between signaling pathways involved in liver development to robustly improve the maturity and yield of pluripotent stem cell-derived hepatocytes. *bioRxiv*. <https://doi.org/10.1101/2020.09.02.280172>.
- Rich, J.N., Guo, C., Mclendon, R.E., Bigner, D.D., Wang, X.F., and Counter, C.M. (2001). A genetically tractable model of human glioma formation. *Cancer Res.* **61**, 3556–3560.
- Sasaki, R., Narisawa-Saito, M., Yugawa, T., Fujita, M., Tashiro, H., Katabuchi, H., and Kiyono, T. (2009). Oncogenic transformation of human ovarian surface epithelial cells with defined cellular oncogenes. *Carcinogenesis* **30**, 423–431.
- Schindelin, J., Arganda-Carreras, I., Frise, E., Kaynig, V., Longair, M., Pietzsch, T., Preibisch, S., Rueden, C., Saalfeld, S., Schmid, B., et al. (2012). Fiji: an open-source platform for biological-image analysis. *Nat. Methods* **9**, 676–682.
- Schreiber, R.D., Old, L.J., and Smyth, M.J. (2011). Cancer immunoeediting: integrating immunity's roles in cancer suppression and promotion. *Science* **331**, 1565–1570.
- Shultz, L.D., Brehm, M.A., Garcia-Martinez, J.V., and Greiner, D.L. (2012). Humanized mice for immune system investigation: progress, promise and challenges. *Nat. Rev. Immunol.* **12**, 786–798.
- Singh, S.K., Hawkins, C., Clarke, I.D., Squire, J.A., Bayani, J., Hide, T., Henkelman, R.M., Cusimano, M.D., and Dirks, P.B. (2004). Identification of human brain tumour initiating cells. *Nature* **432**, 396–401.
- Smith, R.C., and Tabar, V. (2019). Constructing and deconstructing cancers using human pluripotent stem cells and organoids. *Cell Stem Cell* **24**, 12–24.
- Tatum, A.M., Mylin, L.M., Bender, S.J., Fischer, M.A., Vigliotti, B.A., Tevethia, M.J., Tevethia, S.S., and Schell, T.D. (2008). CD8+ T cells targeting a single immunodominant epitope are sufficient for elimination of established SV40 T antigen-induced brain tumors. *J. Immunol.* **181**, 4406–4417.
- Visvader, J.E. (2011). Cells of origin in cancer. *Nature* **469**, 314–322.
- Voabil, P., De Bruijn, M., Roelofsen, L.M., Hendriks, S.H., Brokamp, S., Van Den Braber, M., Broeks, A., Sanders, J., Herzig, P., Zippelius, A., et al. (2021). An ex vivo tumor fragment platform to dissect response to PD-1 blockade in cancer. *Nat. Med.* **27**, 1250–1261.
- Wahl, A., and Victor Garcia, J. (2014). The use of BLT humanized mice to investigate the immune reconstitution of the gastrointestinal tract. *J. Immunol. Methods* **410**, 28–33.
- Wang, M., Yao, L.C., Cheng, M., Cai, D., Martinek, J., Pan, C.X., Shi, W., Ma, A.H., De Vere White, R.W., Airhart, S., et al. (2018). Humanized mice in studying efficacy and mechanisms of PD-1-targeted cancer immunotherapy. *FASEB J.* **32**, 1537–1549.
- Wege, A.K., Melkus, M.W., Denton, P.W., Estes, J.D., and Garcia, J.V. (2008). Functional and phenotypic characterization of the humanized BLT mouse model. *Curr. Top. Microbiol. Immunol.* **324**, 149–165.
- Zitvogel, L., Pitt, J.M., Daillere, R., Smyth, M.J., and Kroemer, G. (2016). Mouse models in oncoimmunology. *Nat. Rev. Cancer* **16**, 759–773.

STAR★METHODS

KEY RESOURCES TABLE

REAGENT or RESOURCE	SOURCE	IDENTIFIER
Antibodies		
Pluripotent Stem Cell 4-marker Immunocytochemistry Kit	Life Technologies	Cat# A24881
PE-Cy7 Rat Anti-Mouse CD45 (Clone 30-F11)	BD Biosciences	Cat# 552848, RRID AB_394489
BUV395 Mouse Anti-Human CD45 (Clone HI30)	BD Biosciences	Cat# 563792, RRID AB_2869519
PE-CF594 Mouse Anti-Human CD19 (Clone 2H7)	BD Biosciences	Cat# 562322, RRID AB_11153322
AF700 Mouse Anti-Human CD3 (Clone SP34-2)	BD Biosciences	Cat# 557917, RRID AB_396938
BB515 Mouse Anti-Human CD4 (Clone RPA-T4)	BD Biosciences	Cat# 564419, RRID AB_2744419
BV421 Mouse Anti-Human CD8 (Clone RPA-T8)	BD Biosciences	Cat# 562428, RRID AB_11154035
BV510 Mouse Anti-Human CD33 (Clone P67.6)	Biolegend	Cat# 366610, RRID AB_2566403
APC-H7 Mouse Anti-Human CD14 (Clone M ϕ P9)	BD Biosciences	Cat# 560180, RRID AB_1645464
BV786 Mouse Anti-Human CD56 (Clone NCAM16.2)	BD Biosciences	Cat# 564058, RRID AB_2738569
BV711 Mouse Anti-Human CD25 (Clone M-A251)	Biolegend	Cat# 356138, RRID AB_2632781
BB700 Mouse Anti-Human CD127 (Clone HIL-7R-M21)	BD Biosciences	Cat# 566399, RRID AB_2744279
BUV737 Mouse Anti-Human CD279 (PD-1) (Clone EH12,1)	BD Biosciences	Cat# 612791, RRID AB_2870118
PE Mouse Anti-Human Tim-3 (CD366) (Clone 7D3)	BD Biosciences	Cat# 565570, RRID AB_2716866
BV650 Mouse Anti-Human CD45RA (Clone HI100)	BD Biosciences	Cat# 563963, RRID AB_2738514
PE-Cy5 Mouse Anti-Human CD45RO (Clone UCHL1)	BD Biosciences	Cat# 561888, RRID AB_395885
Rabbit Anti-Human GFAP (Polyclonal)	Dako	Cat# Z0334, RRID AB_10013382
Mouse Anti-Human Vimentin (Clone O91D3)	Biolegend	Cat# 677801, RRID AB_2565911
Rabbit anti-Human CD45 (Clone D9M81)	Cell Signaling Technology	Cat# 13917T, RRID AB_2750898
Mouse Anti-SV40 T Ag (Clone Pab101)	Santa Cruz Biotechnology	Cat# Sc147, RRID AB_628305
Mouse Anti-Human CD8 (Clone HIT8a)	Biolegend	Cat# 300902, RRID AB_314106
Mouse Anti-Human GD2 (Clone 14G2a)	Biolegend	Cat# 357302, RRID AB_2561883
Mouse Anti-Human CD133/1 (Clone AC133)	Miltenyi	Cat# 130-108-062, RRID AB_2725937
Mouse Anti-Human HLA-A,B,C (Clone W6/32)	Biolegend	Cat# 311402, RRID AB_314871
FITC Rat Anti-Mouse CD45 (Clone 30-F11)	BD Biosciences	Cat# 553080, RRID AB_394609
PE/Cy7 Mouse Anti-Human CD45 (Clone HI30)	Biolegend	Cat# 304016, RRID AB_314404

(Continued on next page)

Continued

REAGENT or RESOURCE	SOURCE	IDENTIFIER
PE Mouse Anti-Human CD19 (Clone HIB19)	Biologend	Cat# 302208, RRID AB_314238
APC Mouse Anti-Human CD3 (Clone UCHT1)	Biologend	Cat# 300439, RRID AB_2562045
APC/Cy7 Mouse Anti-Human CD14 (Clone HCD14)	Biologend	Cat# 325620, RRID AB_830693
Nivolumab: Humanized Anti-Human PD-1	Bristol-Myers Squibb	Study# CA209-7AW
Biological samples		
Human: Primary Astrocytes	ScienCell research Laboratories	Cat# 1800
Human: Primary fetal liver and thymus (research ethics committee protocol number 2126)	CHU Sainte-Justine's humanized mice core	N/A
Chemicals, peptides, and recombinant proteins		
Collagenase D	Roche	Cat# COLLD-RO
Human recombinant Laminin 521	BioLamina	Cat# LN521
KnockOut Serum Replacement (KOSR)	Life Technologies	Cat# 10828010
Recombinant Human Activin A	R&D Systems	Cat# 338-AC
CHIR-99021	Stem Cell Technologies	Cat# 72052
Recombinant Human BMP-4	Peprtech	Cat# 120-05
Recombinant Human bFGF	Peprtech	Cat# 100-18B
IWP-2	Tocris	Cat# 3533
A83-01	Tocris	Cat# 2939
Recombinant Human HGF	Peprtech	Cat# 100-39H
dexamethasone	Sigma-Aldrich	Cat# D4902
Recombinant Human Oncostatin M (OSM)	R&D Systems	Cat# 295-OM
Neural Induction Medium	Gibco	Cat# A1647801
Gentle Cell Dissociation Reagent	Stem Cell Technologies	Cat# 100-0485
Geltrex Matrix	Gibco	Cat# A1413301
Recombinant Human EGF	Peprtech	Cat# AF-100-15
N-2 Supplement	Gibco	Cat# 17502-048
GlutaMAX-I supplement	Gibco	Cat# 35050-061
G418 Geneticin (Neomycin selection)	ThermoFisher	Cat# 11811023
Puromycin	Gibco	Cat# A11138-02
7-AAD	Biologend	Cat# 420404
IVISbrite D-luciferin	Perkin Elmer	Cat# 122799
Critical commercial assays		
CytoTune™-iPS 2.0 Sendai Reprogramming Kit	Life Technologies	Ref# A16517
Human Tumor Dissociation Kit	Miltenyi	Cat# 130-095-929
Experimental models: Cell lines		
Human: HEK 293T/17	ATCC	CRL-11268
Human: Passage >25 iPSC lines	CHU Sainte-Justine iPSC cell reprogramming core	N/A
Human: Primary adult skin fibroblasts (research ethics committee protocol number 2017-1476)	This paper	N/A
Human: Primary fetal skin fibroblasts (research ethics committee protocol number 2017-1476)	CHU Sainte-Justine's humanized mice core	N/A

(Continued on next page)

REAGENT or RESOURCE	SOURCE	IDENTIFIER
Continued		
Experimental models: Organisms/strains		
Mouse: NSG: NOD.Cg-Prkdc ^{scid} Il2rg ^{tm1Wjl} /SzJ	The Jackson Laboratory	Cat# 005557
Mouse: NSG-SGM3: NOD. Cg-Prkdc ^{scid} Il2rg ^{tm1Wjl} Tg(CMV- IL3,CSF2,KITLG)1Eav/MloySzJ	The Jackson Laboratory	Cat# 013062
Oligonucleotides		
probe set HNF4A	Thermo Fischer	Hs00230853_m1
probe set AFP	Thermo Fischer	Hs00173490_m1
probe set GAPDH	Thermo Fischer	Hs99999905_m1
probe set Albumin	Thermo Fischer	Hs00609411_m1
probe set ASGR1	Thermo Fischer	Hs01005019_m1
probe set CK19	Thermo Fischer	Hs00761767_s1
probe set CK7	Thermo Fischer	Hs00559840_m1
Recombinant DNA		
psPAX2	Addgene	Cat# 12260
pMDLg/pRRE	Addgene	Cat# 12251
pRSV-Rev	Addgene	Cat# 12253
pMD2.G - VSVG	Addgene	Cat# 12259
pBABE-neo largeTgenomic	Addgene	Cat# 10891
pLenti-RasV12-puro	Laboratory Francis Rodier (CRCHUM)	N/A
pLenti-hTERT	Gift from Dr Francesco Galimi (Salk Institute)	N/A
pQC mPlum XI	Addgene	Cat# 37355
pLenti-Luc-IRES-GFP	Laboratory Elie Haddad (CHUSJ)	N/A
Software and algorithms		
FIJI/ImageJ	Schindelin et al., 2012	RRID:SCR_002285 http://fiji.sc
Graphpad Prism v8.0	GraphPad	RRID:SCR_002798 http://www.graphpad.com/
FACSDiva	BD Biosciences	RRID:SCR_001456 http://www.bdbiosciences.com/instruments/software/facsdiva/index.jsp
FlowJo	FlowJo	RRID:SCR_008520 https://www.flowjo.com/solutions/flowjo
FlowSOM	Gassen et al., 2015	RRID:SCR_016899 https://github.com/SofieVG/FlowSOM

RESOURCE AVAILABILITY

Lead contact

Further information and requests for resources and reagents should be directed to and will be fulfilled by the lead contact, Dr. Christian Beausejour (c.beausejour@umontreal.ca).

Materials availability

This study did not generate new unique reagents

Data and code availability

- This paper does not report Standardized datatypes. All data reported in this paper will be shared by the lead contact upon request.

- This paper does not report original code.
- Any additional information required to reanalyze the data reported in this paper is available from the lead contact upon request.

EXPERIMENTAL MODEL AND SUBJECT DETAILS

Animals and cell lines

- Mice: *In vivo* experiments were conducted in conformity with institutional committee for good laboratory practices for animal research (protocol #669). Male and female mice used in this study (aged between 7-18 weeks) were of the NSG and NSG-SGM3 (expressing human IL3, GM-CSF and SCF) background. All mice were bred onsite and housed in the animal facility at the CHU Sainte-Justine Research Center under pathogen-free conditions in sterile ventilated racks after being originally obtained from the Jackson Laboratory.
- Adoptive transfer (Hu-AT): On the day preceding tumor injection, human adult peripheral blood was harvested from healthy donors after informed consent and immune cell isolation using Ficoll-Paque gradient (GE Healthcare). Buffy coat was recovered for PBMCs while granulocytes were isolated from the gradient pellet: Ficoll-Paque was aspirated and the pellet was broken and resuspended in 38 mL of sterile deionized water for 20 seconds for RBC lysis before addition 2 mL of sterile 20X PBS solution. PBMCs and granulocytes were counted and mixed at 1:1 ratio before injection into mice. 5×10^6 PBMCs and 5×10^6 granulocytes for a total of 1×10^7 WBC were injected intraperitoneally (i.p.) into NSG-SGM3 in 200 μ L total volume. Aged-match NSG-SGM3 without i.p. injections of WBC were used as no-AT controls.
- BLT mice: For BLT-reconstituted mice (Hu-BLT), 6-8-week-old NSG mice were sublethally irradiated with 2 Gy total body irradiation using a Faxitron CP-160 before surgical implantation of 1-2mm³ human fetal thymus under the kidney capsule and intravenous injection of 5×10^5 CD34+ hematopoietic stem cells (HSC) isolated from autologous fetal liver as previously described (Shultz et al., 2012). Fetal (16-21 weeks) tissues were obtained after written informed consent (ethical committee of CHU Sainte-Justine, CER#2126). Hematopoietic engraftment was assessed by flow cytometry at 4 and 8 weeks by staining 50 μ L of peripheral blood collected from the saphenous vein. Only mice with high reconstitution at week 8-10 (35%-75% human CD45, >20% CD3) were used in this study. Age and sex-matched non-reconstituted NSG mice are used as negative control. In all cases, mice showing signs of GvHD were removed from analysis.
- iPSC reprogramming: Healthy human donor (males and females) PBMCs or skin fibroblasts were reprogrammed into iPSCs using integration-free based Sendai virus. Low passage primary fibroblasts were used to increase reprogramming efficiency. Following transduction, emerging clones were manually picked and cultured under feeder-free conditions using Geltrex-coated dishes and Essential 8 medium. iPSC clones were maintained in culture for at least 15 passages to ensure stable pluripotency before characterization was conducted by the iPSC – cell reprogramming core facility of CHU Sainte-Justine. Cells were shown to have a normal karyotype and colony to express the human SSEA-4, Sox2, OCT4 and TRA1-60 makers (Benabdallah et al., 2019).
- Isolation and culture of skin fibroblasts: Skin fibroblasts were isolated from either adult skin biopsies or fetal skin segments for Hu-AT or Hu-BLT models respectively. Skin tissues were obtained from consented healthy adult donors or after surgical abortion at around week 20 of pregnancy in accordance with the Bureau d'Éthique à la Recherche du CHU Sainte-Justine (protocol number 2017-1476). In both cases, the tissue was cleaned out to preserve only the dermis and epidermis, triturated into 1-5mm² pieces and digested with collagenase D (Roche) for one hour at 37°C with agitation. The whole mixture was then centrifugated at 400 g for 5 min and washed with DMEM twice. The whole product of digestion was seeded in T150 flasks in DMEM with 10% FBS and 0.2% primocin. Subsequent passages were also maintained in DMEM with 10% FBS and 0.2% primocin.

METHOD DETAILS

Hepatocyte differentiation

Differentiation of human iPSCs into hepatocyte-like cells (HLC) was achieved according to our 30-day long, previously described protocol mimicking liver development (Raggi et al., 2020). In brief, iPSCs were differentiated on laminin-coated plates through consecutive stages (primitive streak, mesendoderm, definitive endoderm, posterior foregut, hepatoblasts and, eventually, HLC). Differentiation was started by changing the medium to RPMI-B27 minus insulin supplemented with 1% KOSR and 100 ng/ml Activin A for 3 days. For the first 2 days cells were also exposed to 3 μ M CHIR-99021. From day 4 for 5 days, RPMI-B27 (minus insulin) medium was supplemented with 20 ng/ml BMP4, 5 ng/ml bFGF, 4 μ M IWP-2, and 1 μ M A83-01. From day 10 to day 15, the medium was changed to RPMI-B27 supplemented with 2% KOSR, 20 ng/ml BMP4, 5 ng/ml bFGF, 20 ng/ml HGF and 3 μ M CHIR-99021. At day 16, the medium was changed to HBM/HCM (minus EGF) medium, supplemented with 1% KOSR, 20 ng/ml HGF, 20 ng/ml BMP4, 5 ng/ml bFGF, 3 μ M CHIR-99021, 10 μ M dexamethasone, and 20 ng/ml OSM for 5 days. From day 20, for 5 days, HBM/HCM medium was supplemented with 1% KOSR, 10 μ M dexamethasone and 20 ng/ml OSM. From day 25, the cells were maintained in HBM/HCM 1% KOSR medium supplemented with 10 μ M dexamethasone. Medium was changed every day for the first 20 days and every other day from day 20 to 30. During all the differentiation process, the cells were kept at 37°C, ambient O₂ and 5% CO₂.

NSC and astrocyte differentiation

Neural Stem Cells (NSC) and astrocytes were differentiated from hiPSCs by first using the PSC Neural Induction Medium (NIM). Briefly, hiPSCs were dissociated into small colonies using the gentle cell dissociation reagent and seeded on Geltrex matrix at 50% confluence in E8 medium. 24h later, E8 medium was replaced with complete NIM (neurobasal medium with neural induction supplement) for 7 days with medium change at days 2, 4 and 6. Resulting Neural stem cells (NSCs) were then expanded for at least 3 passages in neural expansion medium (neurobasal medium/ advanced-DMEM/F12 with neural induction supplement). Resulting cells were considered NSCs after validation of the acquisition of nestin expression and loss of OCT4 pluripotency marker by immunofluorescence. NSCs were maintained in StemPro NSC SFM for further transformation (see below) or differentiated further into the astrocyte lineage. To do so, NPCs were plated on Geltrex in a 6 well plate in StemPro NSC SFM supplemented with 20ng/ml of EGF and bFGF for 2 days before switching to astrocyte differentiation medium consisting of DMEM with 1% N-2 supplement, 1% GlutaMAX-I supplement and 1% FBS with medium change every 3-4 days. Differentiated astrocytes were typically observed on days 5-7. Astrocytes were characterized *in vitro* by immunofluorescence for the expression of GFAP and Vimentin. Briefly, cells were seeded in Geltrex coated Lab Tek chamber slides and fixed 5 days later in 3.7% formaldehyde before permeabilization and blocking using PBS with 0.3M Glycine, 1% BSA, 2.5% Goat Serum and 0.1% Triton X-100 for 30 min at room temperature. Primary anti-GFAP or anti-Vimentin antibodies were used at 1/200 concentration overnight at 4°C and secondary AF488-conjugated anti-mouse Ig at 1/500 for 1 h at room temperature. GFAP-expressing astrocyte populations were subsequently transformed (see below). Flow cytometry was done using anti-CD133/1-PE and anti-GD2-APC.

Lentivirus production

All lentiviral particles were produced by overnight PEI transfection of 293T/17 cells (ATCC CRL-11268) in complete RPMI with 10% FBS with 2nd (psPAX2) or 3rd (pMDLg/pRRE and pRSV-Rev) generation packaging plasmids along with a plasmid encoding the VSV-G envelope. SV40ER was subcloned from pBABE SV40ER from William Hahn (Addgene #10891) into a lentiviral transfer plasmid containing a Neomycin resistance gene (SV40ER-Neo), RasV12 lentiviral transfer plasmid containing a puromycin resistance gene (RasV12-puro) was obtained from Francis Rodier (CHUM, Université de Montréal), hTERT lentiviral transfer plasmid was generated as previously described (Beauséjour et al., 2003), mPlum was subcloned from pQC mPlum XI from Connie Cepko (Addgene #37355) (Beier et al., 2011) into a lentiviral transfer plasmid containing puromycin selection gene, and firefly luciferase IRES-GFP (luc/GFP) lentiviral transfer plasmid was obtained from Elie Haddad (CHUSJ, Université de Montréal).

Cellular transformation

Primary fibroblasts and commercially available primary astrocytes (ScienCell research Laboratories, CA USA) or iPSC-derived cell lines were transformed with lentiviral particles in a sequential order. For fibroblast-derived tumors, cells were transduced overnight with medium containing SV40ER-Neo viral particles. Three days later, G418 selection was added at 300 µg/mL and maintained until control GFP-transduced cells were eliminated. Cells were subsequently transduced with RasV12-puro lentivirus in a similar way. Puromycin selection was started three days post-transduction at 2 µg/mL again with GFP-transduced cells as control. Cells were then transduced overnight with medium containing hTERT lentiviral particles. 2 days later, cells were transduced overnight with mPlum viral particles. All transductions were done in presence of 8 µg/mL polybrene. Cells were subsequently expanded and sorted on FACSArialI in the APC channel for the expression of mPlum. For hepatocyte, astrocyte and NPC-derived tumor cells, lentiviral suspensions were used as well as luciferase/GFP instead of mPlum. However, the initial overnight SV40ER transduction was made at day 16, 22 or 30 of the hepatocyte differentiation protocol (see above), and differentiation was pursued. Cells were passaged on day 32 and RasV12-puro transduction was done once the cells were 70%-80% confluent. Three days later, concomitant G418 and puromycin selection started, still at 300 µg/mL and 2 µg/mL respectively, until individual controls for each antibiotic were eliminated. Cells were subsequently transduced with hTERT then luciferase/GFP and sorted on FACSArialI for GFP expression.

Orthotopic injections and monitoring

All injections and surgical procedures were undergone under aseptic conditions in the CHU Sainte-Justine animal facility. For the subcutaneous injections of fibroblast-derived tumors, 5×10^5 cells were injected in 100 µL of RPMI medium on each flank of isoflurane-anesthetized and previously shaved mice. *In vivo* growth monitoring was done twice weekly on the Q-Lumi *In Vivo* imaging system (MediLumine, Montreal) by fluorescent tracking of mPlum-expressing tumor cells. Fluorescence signal was standardized internally for each picture and normalized for defined parameters using FIJI (Schindelin et al., 2012) macros for picture processing. Tumor signal analysis was measured 1) semi-manually also using FIJI macros and expressed in fluorescence integrated density or 2) by caliper measurements. For checkpoint inhibitor studies, three 6 mg/kg doses of Nivolumab anti-human PD-1 antibody (graciously offered by Bristol-Myers Squibb, New York) were injected i.p. at day 14, 17 and 21 post tumor cell injection. Tumors were excised upon sacrifice and tumor weight and volume were recorded. Mice were sacrificed when tumors reached a maximum of 1500 mm³ or showed signs of distress.

Intracranial injections of astrocyte- or NPC-derived tumors were done using a stereotaxic apparatus (Stoelting). Briefly, mice were anesthetized with 2.5% isoflurane and the cranium exposed by performing a 5-6 mm incision on the scalp. A burr hole was made 2mm posterior and 1mm right of the bregma. A 10 µL Hamilton syringe was then inserted into the hole at a 3mm depth and 1 µL of tumor cell suspension (containing 1.5×10^3 cells) was slowly injected (over a period of 10 seconds). The syringe was maintained

for one minute in the hole before being slowly withdrawn to avoid gushing. The hole was then closed with Vetbond tissue adhesive (3M) before suturing the scalp. Mice were treated with buprenorphine daily for 2 days following surgery and monitored for distress signs. *In vivo* monitoring of tumor growth was done at regular intervals by bioluminescence tracking of firefly luciferase-expressing tumor cells. To do so, a 30 mg/mL solution of D-luciferin was injected i.p. at a dose of 150 mg/kg and imaged after 10 min without filters on the Q-Lumi *In Vivo* Imaging System. Signal normalization and analysis was done automatically for all time points using FIJI macros and expressed in radiance (photons \cdot s⁻¹ \cdot sr⁻¹ \cdot cm⁻²) integrated density (Area \cdot mean intensity).

Intrahepatic injections of iPSC-derived hepatic cells were done as follows: Briefly, mice were anesthetized with 2.5% isoflurane and a 15 mm incision was made underneath the ribcage on the left ventral flank. A small incision was made in the peritoneal lining to expose the left hepatic lobe. Using a glass capillary, a 10 μ L (containing 1 or 5 \times 10⁵ cells for donor A and donor B respectively) injection was made at about 2 mm depth in the liver lobe. Incisions were sutured, and the animal was treated with buprenorphine daily for 2 days following procedure. *In vivo* monitoring of tumor growth was done at regular intervals by bioluminescence tracking of firefly-luciferase expressing tumor cells as described above.

Histological analysis and staining

Whole organs or tumor tissues were placed in 4% formaldehyde for at least 48 h before dehydration, paraffin inclusion, and sectioning. Routine hematoxylin eosin saffron (HES) staining was performed and analyzed by a pathologist. Subsequent immunohistological staining of samples were done following clinical protocols by CHU Sainte-Justine's clinical histology department. For immunofluorescent staining, whole organs or tumor tissues were flash frozen on dry ice after harvest. 6-10 μ m-thick sections were made on a cryostat (Leica) and deposited on gelatinized slides and immediately fixed and permeabilized in 95% EtOH. Immunofluorescent staining was performed against human CD45, human CD8, SV40 LargeT antigen, HLA-A,B,C and GD2 with AlexaFluor 488 or 594 secondary antibodies and DAPI counterstain.

Immune infiltrate characterization

Tumors were excised from mice and peripheral blood was harvested at sacrifice. Tumors were digested using the human Tumor Dissociation Kit (with enzymes H and A only to avoid epitope losses) and the GentleMACS Octo Dissociation with heaters. Cells were then filtered on 70 μ m MACS SmartStrainers and washed as per manufacturer's protocol using RPMI with 10% FBS. Cells were then stained with antibodies for analysis by flow cytometry of tumor infiltrating immune cells (tTICs) against the following targets: humanCD3-AF700, humanCD33-BV510 and humanCD25-BV711 and mouseCD45-PE/Cy7, humanCD45-BUV395, humanCD19-PE/CF594, humanCD4-BB515, humanCD8-BV421, humanCD14-APC/H7, humanCD56-BV786, humanCD127-BB700, humanPD-1-BUV737 and humanTim3-PE. Blood samples from the same animals were also stained with the same antibody panel before red blood cell lysis using BD Pharm Lyse lysis buffer. All results were acquired using a BD LSRFortessa. Data analysis was done on FlowJo V10. For tSNE dimensionality reduction analysis, tumor and blood immune cells were subsetted and pooled to obtain a representative sample of 20 000 cells. Dimensionality reduction was done using FlowJo's tSNE implementation and the FlowSOM algorithm (Gassen et al., 2015) was used to identify clusters in an unbiased manner.

QUANTIFICATION AND STATISTICAL ANALYSIS

Student's t-test, one and two-way ANOVA with Šidák's multiple comparison post-tests were done using GraphPad Prism 8.0. All results are presented as the mean \pm SEM. The number of samples analyzed is indicated on the figure legends and represent an individual mouse unless specified otherwise. *p<0.05, **p<0.01, *** p<0.001, ****p<0.0001.